

Article

Effect of Iron Chloride (II) on Bentonites under Hydrothermal Gradients: A Comparative Study between Sodium Bentonite and Calcium Bentonite

Carlos Mota-Heredia, Jaime Cuevas  and Raúl Fernández * 

Department of Geology and Geochemistry, Faculty of Sciences, Autonomous University of Madrid, Cantoblanco, 28049 Madrid, Spain; carlos.mota@uam.es (C.M.-H.); jaime.cuevas@uam.es (J.C.)

* Correspondence: raul.fernandez@uam.es

Abstract: This study investigates the performance of two bentonite materials, specifically MX-80 (Na-bentonite) and FEBEX (Ca-Mg-Na-bentonite), employed as engineered barriers in deep geological disposal facilities for the isolation of high-level radioactive waste, contained in metallic canisters. Experiments conducted at the laboratory scale focused on the interaction of these bentonites with FeCl₂ powder, used as a soluble iron source, to observe enhanced alteration of the bentonite. The experiments were carried out under a hydrothermal gradient. A dominant Na-Cl-SO₄ saline solution was put in contact with the compacted bentonites from the top, while a constant temperature of 100 °C was maintained at the bottom using a heater in contact with the layer of FeCl₂. The experimental cells were examined after six months of interaction. Various changes in the physical and chemical properties of the bentonites were observed. An increase in the water content, a reduction in the specific surface area and cation exchange capacity, changes in the distribution of aqueous species, and the formation of secondary minerals were observed. Reaction products formed at the bentonite interface with FeCl₂, primarily comprising akaganeite, goethite, and hematite. The smectites showed evident structural modifications, with an enrichment in iron content, and a shift in the exchangeable ion distribution in the case of MX-80 bentonite. This work provides valuable insights into the complex interactions between bentonite barriers and materials that dissolve iron, serving as proxies for deep geological disposal environments and indicating the potential long-term behavior, taking into account higher concentrations of dissolved iron than those expected in a real repository.

Keywords: bentonite; metallic canister; hydrothermal gradient; DGR; corrosion



Citation: Mota-Heredia, C.; Cuevas, J.; Fernández, R. Effect of Iron Chloride (II) on Bentonites under Hydrothermal Gradients: A Comparative Study between Sodium Bentonite and Calcium Bentonite. *Minerals* **2024**, *14*, 132. <https://doi.org/10.3390/min14020132>

Academic Editor: Gianvito Scaringi

Received: 14 December 2023

Revised: 20 January 2024

Accepted: 22 January 2024

Published: 25 January 2024



Copyright: © 2024 by the authors. Licensee MDPI, Basel, Switzerland. This article is an open access article distributed under the terms and conditions of the Creative Commons Attribution (CC BY) license (<https://creativecommons.org/licenses/by/4.0/>).

1. Introduction

Bentonite is a type of clay composed primarily of montmorillonite, which is a phyllosilicate mineral with a layered structure and belongs to the smectite group [1]. Montmorillonite has a layered structure, which confers interesting properties such as a swelling ability, a high cation exchange capacity (CEC), and low hydraulic conductivity. Additionally, montmorillonite exhibits high chemical stability, which is an important barrier property in terms of interaction with other barrier materials [2,3]. These properties make bentonite an excellent material to use as a buffer or backfill material in deep geological repositories (DGRs) for radioactive waste [4–7].

The MX-80 and FEBEX bentonites contain 3–4 wt.% of total Fe, included in accessory minerals but primarily as structural iron in montmorillonite, most of it as Fe^{III} (~80% in MX-80) and the remainder as Fe^{II}. The redox properties of iron can affect the properties of the bentonite barrier. For example, under reducing conditions, Fe(III) can be reduced into Fe(II), increasing the layer charge, which can result in a decrease in the swelling capacity [8]. Redox transitions can also affect the hydraulic conductivity and layer charge of the clay. A reduction of Fe(III) into Fe(II) in the dioctahedral layer increases the layer charge, which promotes an increase in the CEC too [9–11].

Depending on a country's nuclear waste policy, high-level waste (HLW) can be isolated using copper, carbon steel, or different alloys [12–14]. The corrosion rate depends on the metallic composition of the canister, as well as other factors, such as the bentonite and the geological conditions in the host rock [15]. The corrosion mechanisms of carbon steel in a deep geological repository of radioactive waste involve several complex processes. The repository environment is characterized by high temperatures, elevated pressure, and the presence of various aqueous chemical species, including dissolved oxygen and highly reactive ions, such as chlorides or sulphates under oxic conditions [7]. These conditions can lead to the initiation and propagation of corrosion, and this could compromise the integrity of the metallic waste container and release radioactive materials into the near field [7,10].

The initial stage of corrosion involves the formation of an oxide layer on the steel surface. This layer can provide some protection against further corrosion, preventing the diffusion of oxygen and other species into the underlying steel. Under anaerobic conditions, the oxide layer can be modified, and corrosion may occur according to an electrochemical process involving the transfer of electrons from the steel surface to dissolved oxygen, generating H_2 or other oxidants in the surrounding environment, leading to the formation of corrosion products such as iron oxides and hydroxides [16].

The presence of chlorides or sulphates can accelerate the corrosion processes under oxic conditions by increasing the rate of electron transfer and promoting the dissolution of the protective oxide layer. Additionally, the high temperatures and pressure in the repository environment can enhance the mobility of the aqueous species and the diffusion of the corrosion products. Under these conditions, the iron in the bentonite can interact with the surrounding environment, leading to the formation of various iron minerals, including magnetite (Fe_3O_4). In addition to magnetite, other iron minerals may also form or be present in the bentonite, including hematite (Fe_2O_3) and goethite ($FeO(OH)$) [17,18]. These minerals can interact either via dissolution and reaction (dissolved Fe adsorption) [19,20] or bridging the octahedral sheet extremes of the montmorillonite in the bentonite, affecting properties such as its swelling capacity, layer charge, or cation fixation [11], and potentially altering its ability to act as a barrier [21,22].

Two types of experiments have been traditionally used to study iron–bentonite interactions: in situ experiments, which are conducted under realistic disposal conditions in underground galleries, and laboratory experiments, which enable controlled experiments under a wider range of experimental conditions, including elevated temperature and hydration [23–27]. A long-term in situ corrosion experiment was conducted in Opalinus Clay at the Mont Terri Underground Research Laboratory (Switzerland), where carbon steel coupons were embedded into MX-80 bentonite. The samples showed the development of a reddish–brown corrosion front or halo around the corroding metal interface. This was attributed to an increase in Fe (II/III) in the bentonite matrix. SEM/EDX measurements confirmed the presence of iron in the halos. These halos were the products of aerobic corrosion at the first stage with oxygen available, rather than the green or black corrosion products formed during the anaerobic corrosion of iron, due to oxygen consumption [25]. Similar phenomena have been reported in a similar corrosion experiment conducted in crystalline rock [15].

In addition to the in situ corrosion experiments described above, several laboratory-based experimental studies have been conducted in the past with the objective of characterizing the changes in the chemical composition and microstructure of the bentonite in close proximity to corroding carbon steel [28–30]. The analysis of the steel–bentonite interface revealed that microfractures in the bentonite occurred close to the corroding surfaces, which were enriched in iron. The corrosion product layer at the surface of the carbon steel was predominantly composed of sub-stoichiometric magnetite or a mixed-phase spinel (e.g., $Fe_{3-x}M_xO_4$) with the possible presence of carbonate minerals. This complex microstructure of the corrosion product layer has been observed in both in situ and laboratory experiments.

The smectite particles close to the metallic corroding surface may also be enriched in Fe due to the Fe–bentonite interaction [28,31]. The metallic corrosion layer composition can

be modified by corrosion products due to the incorporation of chemical species such as carbonates, silicates, and sulfides, as a result of the dissolution of the primary bentonite minerals. This could potentially drive further mineral transformations [7].

The corrosion of steel in contact with bentonite in in situ experiments is commonly understood to occur in two stages: first, an aerobic stage where Fe^{3+} and corrosion products are generated on the steel surface, followed by an anaerobic stage, where Fe^{2+} is generated after oxygen is depleted from the system. During the anaerobic phase, authors agree that Fe^{2+} diffuses into the bentonite and interacts primarily through ion exchange [25,29,32,33]. Conversely, Fe^{3+} was mainly found near the steel–bentonite interface, a few centimeters (<4.5 cm) inside the bentonite, in a long-term experiment that ran for nearly 20 years [22]. The hindrance of Fe^{2+} diffusion by the oxygen present in the bentonite was proposed as the mechanism for this phenomenon. Laboratory batch experiments performed with bentonite and native iron at 60 °C for 1 month showed that corrosion can occur anaerobically, even under laboratory conditions [25]. As a result, Fe^{2+} was oxidized into Fe^{3+} and precipitated mainly as goethite, when it diffused into the aerobic zone of bentonite [25,29].

Wersin and Kober [16,27] proposed a corrosion mechanism for the iron–bentonite interaction comprising four stages: (0) Formation of a thin magnetite layer on carbon steel and prevailing structural Fe(III) in the smectite component at low moisture; (1) Fe(III) oxide formed, whether anhydrous, such as hematite and maghemite, or oxyhydroxides, such as goethite and lepidocrocite, depending on the bentonite moisture content; and (2) the thickness of the corrosion layer increases and the transfer of O_2 and H_2O into the steel decreases. Anaerobic corrosion arises within the corrosion layer, generating Fe(II) and resulting in the formation of magnetite and siderite in the bentonite interface. Additionally, there is rapid electron transfer across the corrosion layer, leading to Fe(II) generation at the interface of the corrosion layer/bentonite, which then reacts with the remaining O_2 to produce further Fe(III) oxides. From this stage onward (stage 3), anaerobic conditions are established, and the corrosion of the steel continues to create Fe(II) and magnetite/siderite with Fe(II), diffusing into the bentonite farther from the iron contact and amassing in the clay, controlled by sorption processes, followed by oxidation. The transfer process probably involves redox reactions with the structural Fe(III) and previously formed (and pre-existing) Fe(III) oxides near the interface, though the precise mechanism of this transfer process remains to be established [16]. The accumulated Fe^{3+} near the interface is slowly displaced toward the bentonite. Leupin et al. [30] compiled several reaction paths justifying the anoxic corrosion model producing Fe(II) and Fe(III) oxides and hydrogen at the corrosion interface. Mobile iron species can interact with the bentonite and lead to the formation of iron-rich clay minerals and precipitates around the steel–bentonite interface. The dissolved Fe^{2+} released at micro-molar concentrations due to the corrosion of steel canisters can interact with montmorillonite and change the mineral oxide reduction state, potentially affecting relevant mineral properties. Additionally, ferrous iron may compete with cationic radionuclides for the cation exchange capacity of the clay, which could result in a reduction in the sorption capacity of the bentonite [31].

The solubility of reduced iron is controlled by solid phases like green rust, magnetite, or $\text{Fe}(\text{OH})_2$ [34]. The presence of Fe(II) could provide adsorption–desorption phenomena through exchange with other cations like Na, Ca, or Mg [35]. This Fe(II) can be exchanged in the form of Fe^{2+} , as well as FeCl^+ [34].

Despite the fact that long-term studies in underground laboratories performed for several years to decades have shown limited corrosion effects on the bentonite barrier, there is not a complete picture of the prevailing Fe II and III minerals controlling the evolution of mineralogical alterations in bentonite [15,24,30]. Thus, further research is needed to better understand these interactions and their potential impact on the safety of nuclear waste disposal in clay environments [36]. In order to enhance the mineralogical expression of the Fe(II) interaction environment and study the potential oxidation and mobility of iron aqueous species in simulated initial anaerobic conditions, in the present study, FeCl_2

powder has been placed in contact with bentonite, in substitution of steel, as previously used by Mota-Heredia et al. [37].

2. Materials and Methods

2.1. Experimental Setup

The experiments were performed in a glove box with an inert atmosphere of N₂ in order to prevent the oxidation of the FeCl₂ powder before starting the experiments. FeCl₂ was introduced into the cell until a thickness of uncompressed powder of ~4 mm was achieved, measured using a vernier caliper. The amount of FeCl₂ inserted into the cell was calculated by the difference in the weight of the reagent container. Thereafter, bentonite powder was introduced on top of the FeCl₂ and compacted using a hydraulic press. Bentonite blocks were theoretically compacted to attain a dry density of 1.65 g·cm⁻³, 21 mm in height, and 50 mm in diameter. Each portion of bentonite powder was weighed beforehand, with a mass of 76.9 g FEBEX bentonite and 72.9 g MX-80 bentonite. These amounts were determined by considering the natural moisture content of each bentonite sample stored in the laboratory, 12.5 wt.% for FEBEX and 7.2 wt.% for MX-80. The experiments were performed using hydrothermal cells designed in-house, previously used in Mota-Heredia et al. [37]. A complete description of the experimental setup is provided in the reference therein. The cells contain a cylindrical Teflon carcass inserted within a steel ring that minimizes the deformation in case of bentonite swelling. The FeCl₂ powder was placed at the bottom of the cells and heated at a constant temperature of 100 °C using a steel plate. A thermal gradient was established in the bentonite column, which was 100 °C at the bottom and 40 °C at the hydration zone, the upper part of the cells, where a synthetic saline solution representative of a generic clayey formation was pressurized (approximately at 1.5 bar) toward the bentonite. The experiments were carried out in a glove box, under a N₂ atmosphere, to prevent any contact with atmospheric O₂ during the experiment in case of failure and during the dismantling of the cells.

Although bentonite powder was inserted into the cells under a N₂ atmosphere in the glove box, aerobic conditions due to the trapped air within the bentonite aggregates under the stock conditions were assumed to prevail. This, along with the oxic conditions of the saline solution, which was not degassed, led to initial aerobic conditions within the cells, mimicking the conditions that would occur in a repository during the operational phase when the engineered barriers are installed.

2.2. Materials

To maintain the hydration in the bentonite, a Na-Cl-SO₄-type synthetic saline solution was used, as described in Mota-Heredia et al. [37]. The main chemical composition of the solution is: Cl⁻ = 38.9 mM, SO₄²⁻ = 13.8 mM, HCO₃⁻ = 3.3 mM, Na⁺ = 44.8 mM, K⁺ = 1.8 mM, Ca²⁺ = 7.5 mM, Mg²⁺ = 5.1 mM, and pH 7.9.

Two types of bentonites were used: MX-80 and FEBEX. MX-80 is a type of Na-bentonite from Wyoming (USA), is considered a standard buffer and backfill material for radioactive waste disposal in various countries, and has been extensively studied in this field [38–41]. It is composed of ~87 wt.% montmorillonite and includes accessory minerals such as quartz, feldspars, pyrite, and gypsum. Fe minerals like magnetite and goethite are present in traces.

FEBEX bentonite is extracted from the Cortijo de Archidona, at the Serrata de Níjar, Almería, Spain [42,43], and is considered the standard buffer material for radioactive waste disposal in Spain [44]. This bentonite contains ~85 wt.% of montmorillonite and accessory minerals such as quartz, cristobalite, calcite, and feldspars. It also contains traces of Fe minerals like magnetite and goethite. Various quantification studies have revealed a relative 10 wt.% error in the smectite content [42,45].

The anhydrous ferrous chloride used in this study was from Acros Organics™ (CAS 7758-94-3) and has 97% purity. It is presented in powder form and its solubility

in water is $644 \text{ g}\cdot\text{L}^{-1}$. The amount of FeCl_2 used for the MX-80 cell was 8.7 g, and 7.9 g was used for the FEBEX cell.

2.3. Sample Segmentation

At the end of the 6-month experimental time, FeCl_2 -bentonite columns were taken apart from the Teflon cells, under a N_2 atmosphere, and hardened in epoxy resin for further sectioning. The cells were cut using a Struers™ Secotom-6 saw (Champigny sur Marne, France), while employing a cooling oil that neither interacts with the samples nor exposes them to atmospheric oxygen. Longitudinal cuts on the cylindrical bentonite samples were made using the Secotom-6 saw, while a cutter was used for transversal cuts. To analyze the reactivity along the hydrothermal gradient, the samples were cut to ensure that enough material was available for each characterization technique, as per the sampling method used in Mota-Heredia et al. [37].

2.4. Analytical Methods

To measure the water content, the sample was heated to a constant weight at $105 \text{ }^\circ\text{C}$, and the mass difference was calculated. The specific surface area (SSA) was determined according to the nitrogen adsorption using a Gemini V analyzer (Waltham, MA, USA) from Micrometrics and calculated using the BET method. The samples were ground and dried at $90 \text{ }^\circ\text{C}$ for 24 hours. Subsequently, the samples were degassed at $90 \text{ }^\circ\text{C}$ for at least an hour using a nitrogen gas stream and analyzed using the 5-point isotherm method [46].

The CEC was determined using the Cu-trien method [47], with the modifications made for clays as in Ammann [48]. The absorbance was measured at 577 nm using a GENESYS 150 UV-visible spectrophotometer from Thermo Scientific (Waltham, MA, USA).

A 0.15 solid:liquid ratio was used to mix the samples with deionized water to obtain the aqueous extracts. The samples were then subjected to 24 h of interaction with water in a shaker, followed by centrifugation for 20 minutes at 10,000 rpm. Finally, the aqueous extracts were filtered using a pore size $<0.45 \text{ }\mu\text{m}$. A Metrohm 888™ titration device (Herisau, Switzerland) was used to determine the pH of the porewater. Analyses of major ions including Na^+ , K^+ , Ca^{2+} , Mg^{2+} , Cl^- , and SO_4^{2-} were performed using a Metrohm 802™ Compact IC (Herisau, Switzerland) plus using ion chromatography.

Longitudinal thin section samples were prepared for scanning electron microscope (SEM) and energy-dispersive X-ray (EDX) analyses. Each sample was freeze-dried using immersion in liquid nitrogen and using a vacuum. After that, the samples were embedded and polished [37]. The samples were coated with Au using a Q150T-S Quorum sputter coater system. Surface and morphology images were captured using a Hitachi S-3000N SEM coupled with an EDX XFlash® 6130 Bruker detector (Madrid, Spain) for semi-quantification analyses of the chemical composition. Internal standard quantitative analyses were used for the EDX quantification. The microscope operated under high vacuum conditions with an accelerating voltage of 20 keV, a lifetime of 40 s, a working distance of 15.0 to 18.5 mm, and a beam current of 300 mA.

A SEM-EDX study was conducted to determine the chemical composition in a longitudinal profile, from the heater to the hydration zone. Greater magnification was applied to the images at the hottest zone where FeCl_2 was placed, while lower magnification was carried out at the central and hydration zones, where the chemical variations were expected to be less significant. Around 20 analyses were conducted over a thickness of 2 mm at the steel-bentonite interface, 15 analyses over a thickness of 3 mm at the hydration zone, and 40 analyses at the intermedium zone over a thickness of 16 mm, although the number of analyses and thickness may vary slightly from one sample to another. The EDX analyses were used to observe the migration of FeCl_2 along the bentonite and the concentration changes in elements such as Mg, Ca, Na, K, Cl, S, and Fe. The data were processed by removing C and O concentrations from the analyses and recalculating the remaining weight percentages. The mineralogy of bentonites was also analyzed on fresh fractured samples to observe the morphologies of the reaction products. Small samples that either fell apart or

were manually separated were used for this study. The error of quantitative EDX analyses was between 10% and 20% depending on the type of preparation of samples.

To compare the redox state of Fe along the bentonite blocks, 1,10-phenanthroline was used according to the photochemical method described by Stucki [49,50]. This method allowed discrimination between the ferrous and total iron in the mineral samples. The procedure consists of sampling 50–100 mg dry bentonite and placing it in a propylene tube with 1.8 M H₂SO₄ and 48% hydrofluoric acid, adding 1,10-phenanthroline monohydrate in 95% ethanol as a 10% (wt/wt) solution, and then leaving the tube in a boiling water bath for 30 minutes. This procedure was carried out under red light to avoid photochemical oxidation of the Fe²⁺ into Fe³⁺. At this step, the complexation of Fe with phenanthroline takes place. The sample is neutralized with a solution of 5% (wt/wt) boric acid in water and is diluted with distilled water. After cooling for 15 minutes, an aliquot (1 mL) of the sample solution is taken and transferred into an Erlenmeyer flask, adding 10 mL of distilled water and 1 mL of 10% sodium citrate dihydrate in water. A GENESYS 150 UV-Visible spectrophotometer from Thermo Scientific (Waltham, MA, USA) was used to measure the absorbance at 510 nm.

The Erlenmeyer flask was then stoppered with parafilm to prevent evaporation and left for 72 hours in the light to allow photochemical oxidation of the Fe-phenanthroline. The absorbance is measured again at 510 nm to obtain the total iron content. Fe³⁺ is measured by the difference between the total Fe and Fe²⁺. The calculations were made using the absorptivity obtained by Stucki [49], after observing the same linearity of the phenanthroline absorption. The formula used was $C = \text{Abs} \cdot \epsilon^{-1} \cdot l^{-1}$, where C was the concentration of Fe²⁺ or Fe total in wt.%; Abs the absorbance of the sample; ϵ the absorptivity of the standard solutions; and l the path length (1 cm).

To study the mineralogical changes in the bentonite block and at the FeCl₂ interface, X-ray diffraction (XRD) was conducted using a Bruker D8 DISCOVER (Madrid, Spain) diffractometer with a Ge monochromator and a LYNXEYE XE-T fast detector. The patterns were measured within a 3–70° $\theta/2\theta$ range, with 0.02° angular increments of 2 s. The device was set at 40 kV and 40 mA. To prevent the oxidation of possible reduced compounds, the airtight holder A100B138-B141 from Bruker (Madrid, Spain) was used during all the XRD powder analyses.

Micro-computed X-ray tomography (μ -CT) (Madrid, Spain) was used to analyze the columns for both bentonites, before and after the experimental time. This non-destructive technique enables the observation of how the FeCl₂ powder is distributed along the bentonite and the evolution of the porosity. This analysis was conducted at the Centro Nacional de Investigación de la Evolución Humana (CENIEH) using a MicroCT V|Tome|x S240 Phoenix X-ray from GE Sensing & Inspections Technologies. The parameters used included an isometric voxel size of 40 μ m, over 600 images taken, rotation over the Z-axis, and a voltage of 210 kV. The Dragonfly software from Object Research Systems was used to perform the image treatment.

3. Results

3.1. Physical–Chemical Characterization

The water content increased considerably in both bentonites after six months of reaction. The MX-80 bentonite water content increased from 7 wt.% to ~25–26 wt.%. The trend in FEBEX bentonite was similar, with the water content increasing from 13 wt.% to ~21–24 wt.% (Figure 1). The water content measured in both bentonites was similar along all sections for each bentonite, indicating that the hydration was distributed homogeneously from the top to the bottom of the bentonite columns.

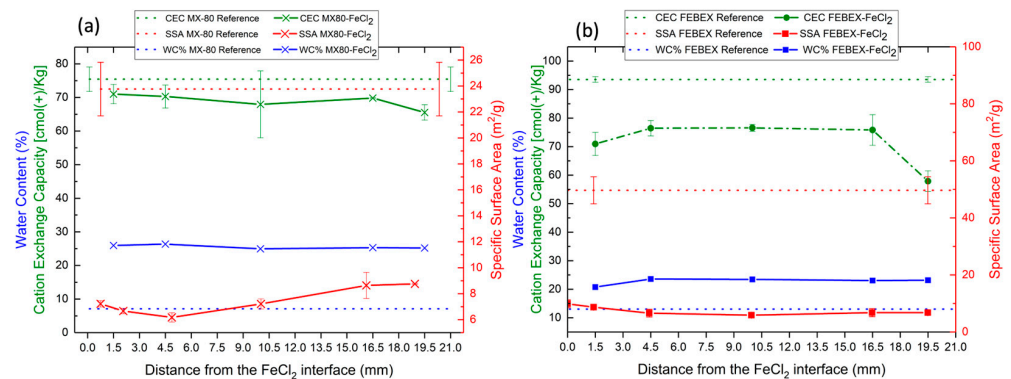


Figure 1. CEC, SSA, and water content evolution measured in vertical sections of bentonite (heater to hydration direction) for (a) MX-80 and (b) FEBEX. The values represent the state after termination of the experiments.

The SSA analyses indicated a significant decrease in both bentonites (Figure 1). The percentage of decrease was ~62%–71% for MX-80 and ~80%–88% for FEBEX; both bentonites decreased in this parameter from $24 \pm 2 \text{ m}^2/\text{g}$ in MX-80 and $50 \pm 5 \text{ m}^2/\text{g}$ in FEBEX bentonites to similar values in the range of $6\text{--}10 \text{ m}^2/\text{g}$.

The CEC also decreased with respect to the reference material (Figure 1). This property was reduced from 75 to 65–71 $\text{cmol}(+)/\text{kg}$ in the MX-80 bentonite and from 94 to 58–76 $\text{cmol}(+)/\text{kg}$ in the FEBEX bentonite.

3.2. EDX Chemical Profiles, Mineralogical and Chemical Characterization

The EDX analyses performed on the polished samples were used to represent the chemical profiles in each bentonite after the experiment. The concentration of the major elements (Fe, Al and Si) remained stable in both bentonites, but compared with the initial data from the raw bentonites (Figure 2a,b), a decrease in Al and Si and an increase in Fe after exposure to the FeCl_2 powder for the MX-80 bentonite are observable. The Fe increases from an averaged $6.5 \pm 1.0\%$ to $9.8\text{--}22.4\%$. The averaged changes in Si, Al, and Fe for the FEBEX bentonite are more moderate than for MX-80. Only a significant increase in Si and, consequently, a decrease in Al is observed neat the heater, at a length of approximately 3–4 mm. The relative Fe content showed only a slight increase compared to the reference value. The averaged Fe increased from $4.6 \pm 0.7\%$ to $7.1\text{--}15.2\%$ in the FEBEX bentonite.

The behavior of Ca and Na in both bentonites was similar, decreasing with respect to their reference values, although there was more dispersion of data for the FEBEX bentonite, and the Na concentration increased in the 3 first mm from the heater, from 2 to 4 wt.%. Mg decreased in the MX-80 bentonite but remained at similar values to the reference for the FEBEX bentonite, again considering a larger dispersion of data than for MX-80. The decrease in Na, Ca, and Mg was not net but relative to the increase in Fe, which is observed along the whole column of bentonite. The relative Cl concentration increased largely from a reference value of $0.2 \pm 0.3 \text{ wt.}\%$ in both bentonites to values in the range of 4–10 wt.%. An increase in Cl was observed at 4–5 mm from the interface with the heater for both bentonites, but a Cl increase was also observed for the MX-80 bentonite at both extremes of the column, in contact with the hydration solution and with the FeCl_2 powder near the heater (Figure 2c,d).

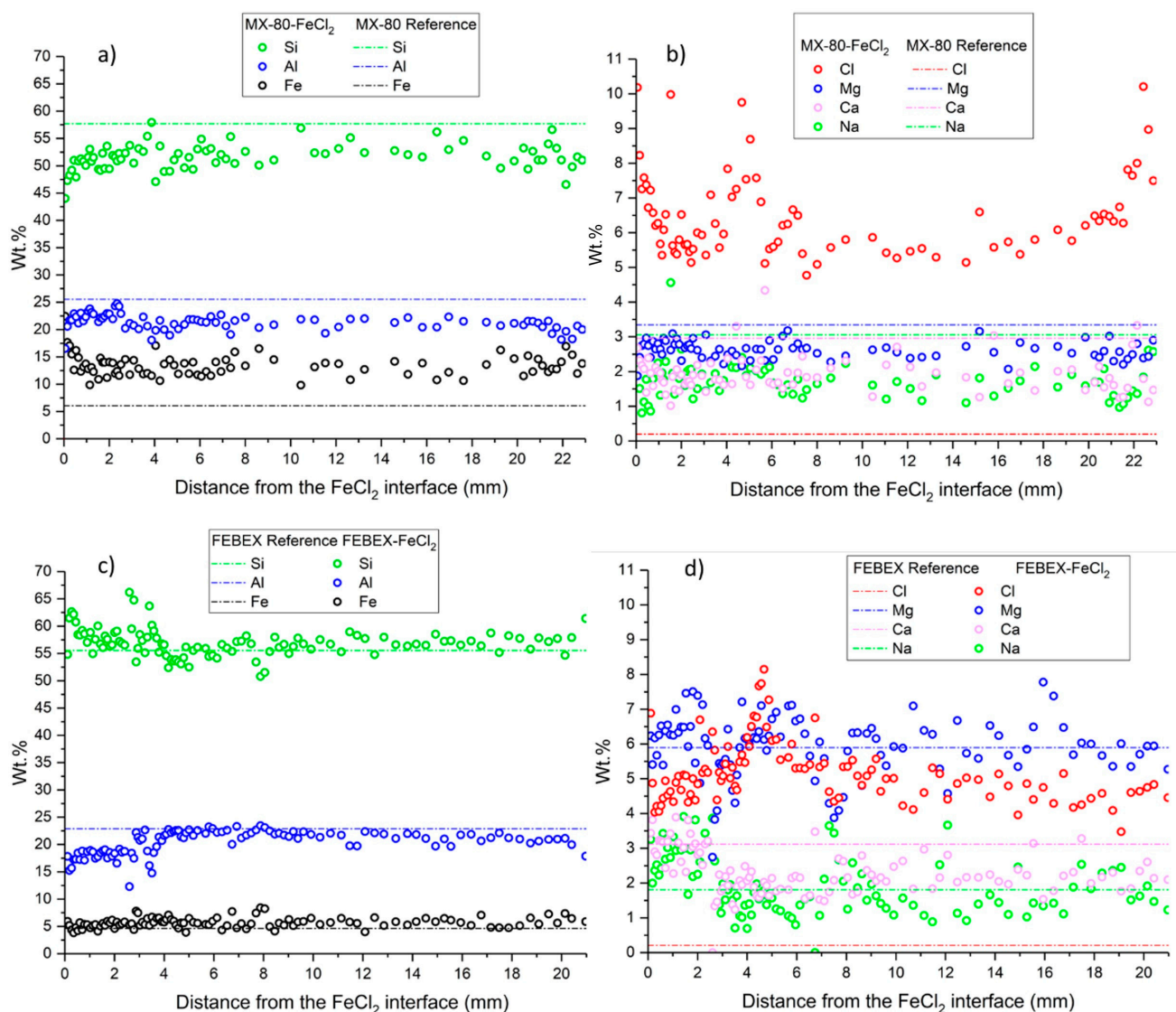


Figure 2. EDX chemical profiles expressed in wt.%: (a) major elements in MX-80 bentonite; (b) minor elements in MX-80 bentonite; (c) major elements in FEBEX bentonite; (d) minor elements in FEBEX bentonite.

The SEM study showed the formation of new mineral morphologies not present in the original bentonites, mainly located in the zones in close contact with the FeCl₂. The external aspect of the clay aggregates in the MX-80 bentonite was modified by the adsorption of iron-containing particles (Figure 3). A rugous texture was observed in those aggregates with a higher content of Fe (representative analysis 1). Representative EDX analysis 2 showed a Si/Fe ratio near 1, like a Fe-rich aluminous silicate phase, presumably a Fe-rich chlorite or serpentine-like mineral (berthierine-like: $(\text{Fe}^{2+}\text{Mg})_{3-x}(\text{Fe}^{3+}\text{Al})_x(\text{Si}_{2-y}\text{Al}_y)\text{O}_5(\text{OH})_4$) [51,52]. Areas rich in Na and Cl (representative analysis 3) were identified. The images captured of the fresh fractures of the MX-80 bentonite close to the FeCl₂ interface (Figure 3) showed iron structures of a spicule form (representative analyses 4 and 5). Additionally, (not shown in Figure 3) punctual framboids of pyrite were observed at the FeCl₂ interface, and the chemical composition was confirmed using the EDX analyses, although it could not be confirmed that these aggregates were neoformed.

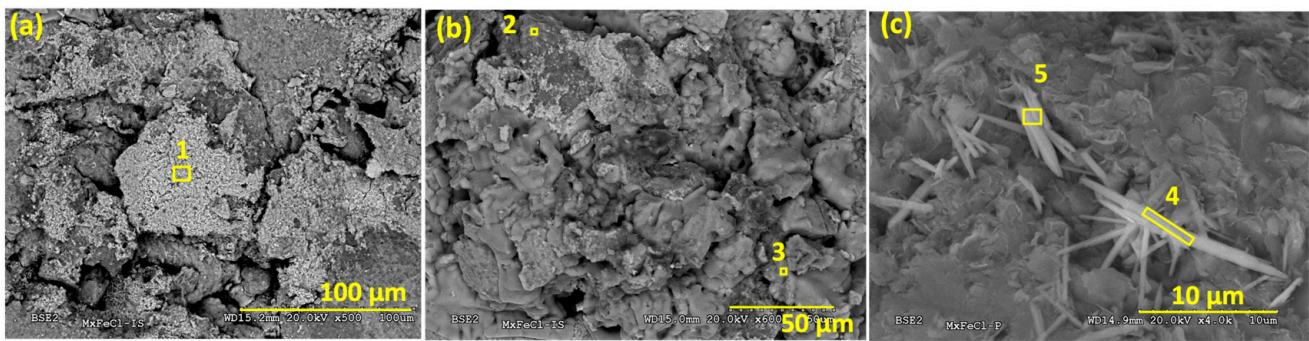


Figure 3. SEM images of fresh fractured samples of MX-80 bentonite: (a) Fe cover of aggregates in bentonite samples near contact with FeCl_2 ; (b) halite precipitation and iron and chloride accumulation in the smectite; (c) Fe spicules in bentonite matrix.

The SEM images and EDX analyses of the fresh fractures close to the FeCl_2 interface in the FEBEX bentonite showed smectite alteration due to the incorporation of Fe and Cl. Figure 4a–c show the aspect of the bentonite aggregates after six months of reaction and the formation of new Fe-rich silicates. The spicules found had a high Fe content (>50%) and more than 10% of Cl was found coating the smectite aggregates (representative analyses 1 and 5). The chemical composition in the areas analyzed using EDX showed Si/Fe ratios ~ 1 in analyses 3, 4, and 6. The composition and textural aspect of the aggregate was similar to chlorites. The color mapping of Figure 4b shows the distribution of Cl, Fe, Si, and Mg (Figure 4c). The sample was coated with Cl and Fe, and the concentration of Mg was notable and related to Si.

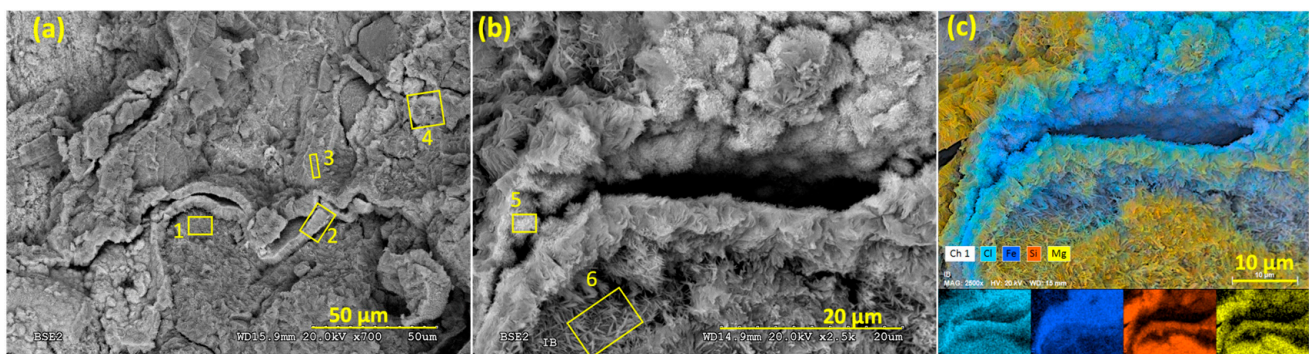


Figure 4. SEM images in fresh fractures of FEBEX bentonite: (a) smectite enriched with Fe and Cl; (b) Fe-Cl spicules on altered smectite; (c) color mapping of Cl, Fe, Si, and Mg distribution on the altered smectite in a fresh fracture of FEBEX bentonite.

1,10-phenanthroline was used as a redox indicator to distinguish between the Fe^{2+} and total Fe and, indirectly, to quantify the Fe^{3+} . Fe^{2+} was almost depleted at a thickness of 2 mm in the MX-80 bentonite at the heated contact with the FeCl_2 (Figure 5a). The Fe^{2+} content in the rest of the bentonite column decreased with respect to the reference concentration (0.53 ± 0.11 wt.%), although the standard deviation for these measurements was large. Fe^{2+} kept close to the reference concentration (0.20 ± 0.16 wt.%) in all sections of the FEBEX bentonite, except at 2–3 mm from the contact with the FeCl_2 , where a sharp decrease was found. In contrast, Fe^{3+} increased in both bentonites with respect to their reference concentrations, indicating a transference from Fe^{2+} into Fe^{3+} (Figure 5b). In the MX-80 bentonite, the maximum concentration of Fe^{3+} was observed at 2–3 mm from the contact with the FeCl_2 , while for the FEBEX bentonite, the highest Fe^{3+} concentration was determined at the contact with the FeCl_2 (10.9 wt.%).

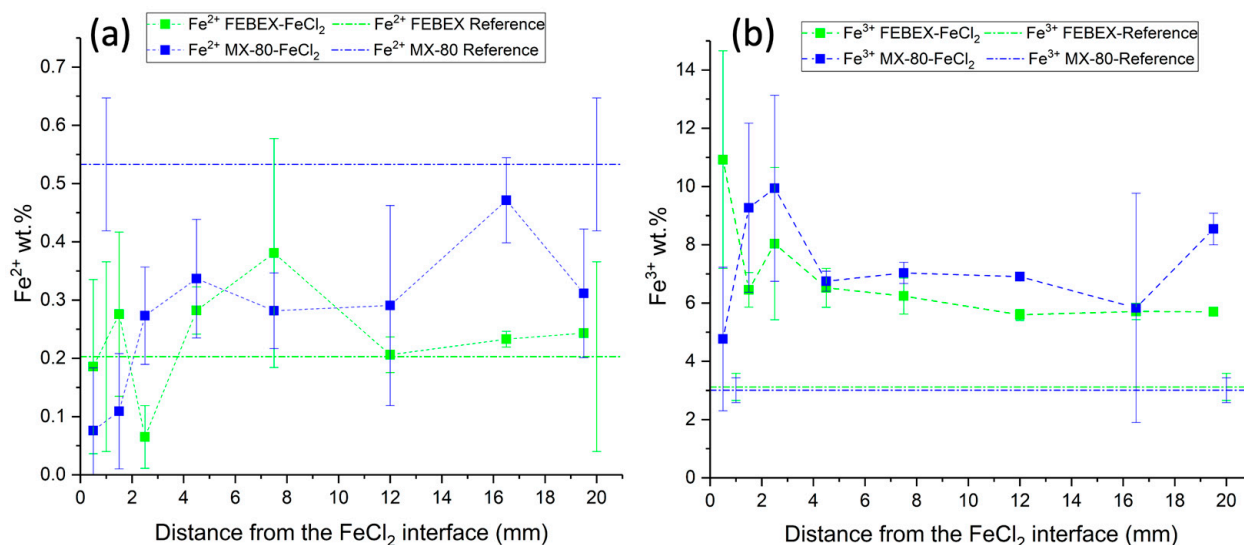


Figure 5. (a) Fe²⁺ concentration (wt.%) along the bentonite columns; (b) Fe³⁺ concentration (wt.%) along the bentonite columns.

The sodium in the MX-80 bentonite presumably changed into Fe²⁺-, Ca²⁺-, and Mg²⁺- in the exchange complex, as the basal spacing shifted from 12.5 to 15.0–15.3 Å after 6 months of reaction (Figure 6a). The reference MX-80 sample showed a basal spacing with two main reflections at 14.3 and 12.5 Å, characteristic of montmorillonite. Gypsum (7.6 Å reflection) decreased in intensity with a decreasing distance from the FeCl₂ layer. However, anhydrite appeared (at 3.5 Å) in several sections, from <1 mm to 15 mm from the heater. Muscovite, albite, and plagioclase were detected as accessory minerals because of their presence in the reference bentonite. Halite (2.82 Å) was identified in all sections. Pyrite was identified in all samples (2.7 Å and 1.63 Å), except in the section at 6–9 mm. Iron chloride was detected at 3.97 Å in all samples, with a higher intensity in the hottest sections (0 to 6 mm from the contact with the FeCl₂). Iron carbonate hydroxide, designated as green rust, was detected in the sample close to the FeCl₂ contact (<1 mm) at 7.53 Å. Akaganeite was detected all along the bentonite column at 7.48 Å. Ankerite was detected close to the interface (<1 mm) at a low intensity at 2.90 Å. Goethite (4.19 Å) was identified in a range from 0 to 15 mm and hematite in the samples close to the FeCl₂ contact (<6 mm) at 2.69 Å.

The FEBEX bentonite kept its basal (001) reflection at 15 Å (Figure 6b), as in the reference sample. Accessory minerals like plagioclase, albite, muscovite, and cristobalite were found in all sections at variable intensities. Goethite appeared in sections at a distance less than 15 mm from the FeCl₂ contact. Iron chloride was detected all along the bentonite column, decreasing in intensity with an increase in the distance from the FeCl₂ contact. Green rust and ankerite were barely distinguished close to the interface with the FeCl₂. Hematite was detected in the hottest sections (<3 mm). Akaganeite [Fe³⁺O(OH,Cl)] was detected at low intensity in all samples. The identification of certain minerals was difficult due to the complexity of the samples and the background of the diffractograms because of the diversity of the mineral phases and low crystallinity grade.

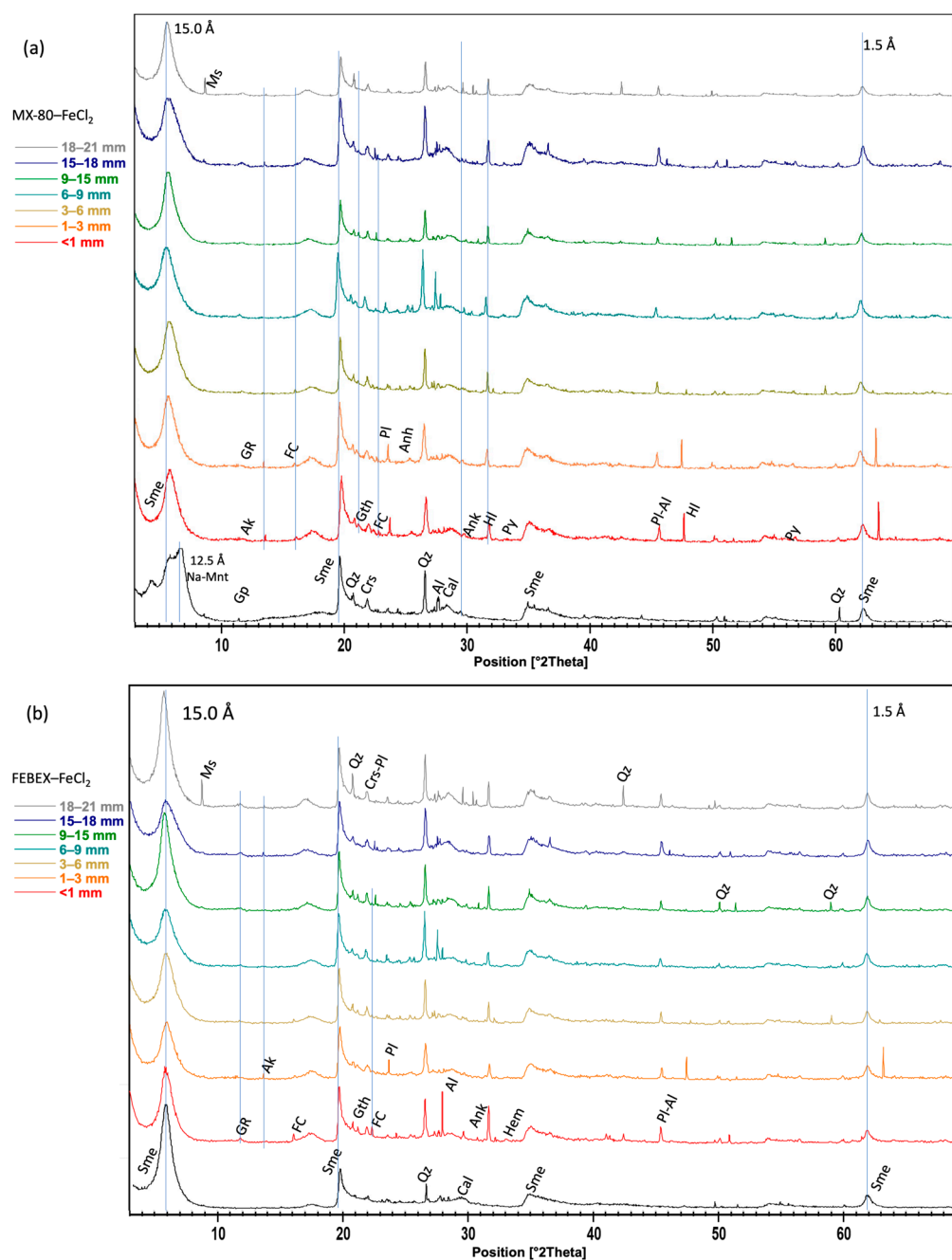


Figure 6. (a) XRD of MX-80 sections parallel to the heater; (b) XRD of FEBEX sections parallel to the heater. Ak: akaganeite; Al: albite; Anh: anhydrite; Ank: ankerite; Cal: calcite; Crs: cristobalite; FC: iron chloride; Gp: gypsum; GR: “green rust”; Gth: goethite; Hem: hematite; HI: halite; Mag: magnetite; Mgh: maghemite; Ms: muscovite; Na-Mnt: sodium montmorillonite; Pl: plagioclase; Py: pyrite; Qz: quartz; Sme: smectite.

The aqueous extracts indicated the redistribution of soluble ions after the reaction. Figure 7a shows the concentrations analyzed in the aqueous extracts of the MX-80 bentonite as a function of the distance from the FeCl₂ contact. Ca²⁺, Mg²⁺, K⁺, Fe^{2+/3+}, and SO₄²⁻ ranged between 62 and 560 mM. Na⁺ was measured between 1.15 and 1.35 M. Chlorides were measured in a range of 3.98–4.67 M. The maximum concentration was determined for the section between 15 and 18 mm from the FeCl₂ contact.

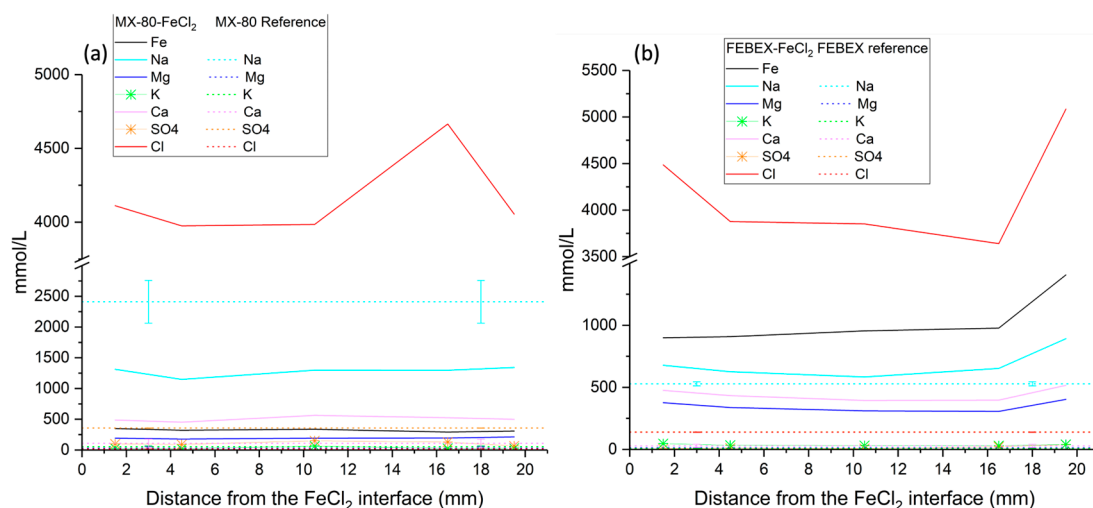


Figure 7. Concentrations of aqueous extract along the bentonite column, expressed in mmol/L. (a) for MX-80 bentonite and (b) for FEBEX bentonite. References values represented by dot lines.

In the FEBEX bentonite (Figure 7b), the chlorides were concentrated at both extremes, in the sections closest to the hydration and to the heater. Cl^- concentrations of 5.08 and 4.49 M were determined at both ends, respectively. Aqueous iron species also presented high concentrations in the FEBEX bentonite, within a range between 0.90 and 1.40 M. The rest of the ions analyzed were found in a range of 7–900 mM, and their concentrations can be arranged in the following decreasing order: Na^+ , Ca^{2+} , Mg^{2+} , K^+ , SO_4^{2-} .

3.3. Micro-X-ray-Computed Tomography (μ -CT)

Determinations using μ -CT in both bentonite columns before the experimental setting and just after the experimental time, before dismantling, were used to quantify the changes in the cell volume and porosity at the macroscale ($>12.5 \mu\text{m}$ approximately) and to observe the FeCl_2 migration considering the contrasted changes in the bright iron mass deposited initially. A thin layer of FeCl_2 powder was initially present at the bottom of the cells, and macropores perpendicular to the compaction direction were observed in the bentonite columns (Figure 8a,c). The initial macropores are the result of the compaction process, as the bentonite powder was uniaxially pressed on top of the FeCl_2 powder initially. Large convex pores were initially observed for the MX-80 bentonite. After six months of FeCl_2 reaction and due to the conditions imposed in opposite directions, hydration and heat, which created a hydrothermal gradient, the FeCl_2 powder was barely distinguishable at the bottom of both cells. The initial large pores observed in the bentonite closed after 6 months due to hydration. A homogeneous distribution of small pores in MX-80 after 6 months was observed, although in the case of FEBEX, it was not observed. These porosity changes were observed along the whole columns, showing the impact of the reaction with FeCl_2 after 6 months (Figure 8b,d). The MX-80 bentonite decreased in its macroporosity (Figure 8a,b) from 6.6% at the initial stage to $<1\%$, measured relative to the total volume of macropores of 3.4 cm^3 after 6 months. The diameter did not change during the experiment (51.2 mm measured), but the height increased from 19.2 mm to 21.8 mm (11.9% increase) after the reaction. Although the pores reduced substantially, the internal contour of the cylindrical cells and the upper and lower boundaries of the bentonite showed a defined path, where the fluid flow could have preferentially been transported during the initial stage, before saturation. It seems that during the initial hydration, the water flow reached the interface with Fe(II) . The calculated macroporosity in the FEBEX bentonite decreased from $\sim 4\%$ to $<1\%$, considering a final total volume of macropores of 1.7 cm^3 . The dimensions of the column did not change in diameter (50.1 mm) but increased in height from 19.9 mm to 21.1 mm ($\sim 5\%$). The initial FeCl_2 powder dissolved and migrated considerably through

the bentonite cells, as a much lower amount of FeCl_2 was observable at the end of the experiments.

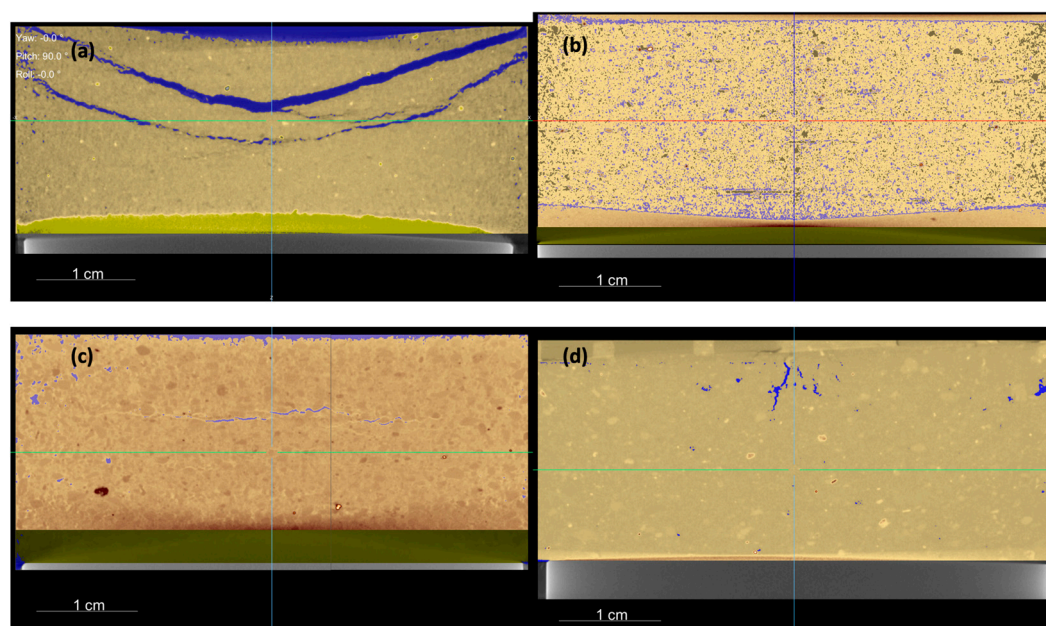


Figure 8. μ -CT cross-section images of experiments: (a) MX-80- FeCl_2 before reaction; (b) MX-80- FeCl_2 after 6-month reaction; (c) FEBEX- FeCl_2 before reaction; (d) FEBEX- FeCl_2 after 6 months of reaction. Porosity (blue), bentonite (light yellow), FeCl_2 powder (dark yellow), steel heater (gray).

Videos S1–S4 show the porosity evolution in each cell and the distribution of FeCl_2 powder before and after 6 months of reaction (see Supplementary Materials). The high atomic mass of the metal elements present in the steel heater generated visual artefacts in the representations that complicate better visualization at the bottom of the cells.

4. Discussion

The physical–chemical properties of both bentonites were modified. The water content increased until the saturation state, and the CEC and SSA were reduced due to the hydrothermal gradient, as confirmed in previous studies [26,37]. The water content increased in both experiments due to the constant low pressure from the hydration tank, which permitted progressive water uptake from the bentonite. As observed in the μ -CT study, not only did the upper part of the bentonites display a larger porosity due to the initial columns setting and the contact with the hydration solution but this also occurred in the internal boundaries of the Teflon cells in contact with the bentonites. Therefore, the water migration from the top could have reached the bottom of the cells during the first stages, creating a preferential path for hydration, which could also have promoted the dissolution of the FeCl_2 and its transport along the bentonite column. At a heater temperature of $100\text{ }^\circ\text{C}$, water vapor might have been generated and moved through pores to condense in cooler regions [53]. After 6 months of reaction, the water content was similar in both bentonites, and, according to the mass balance calculations, the initial free pore space present in both cells was not only fully saturated by the incoming hydration solution but rather the cells had to increase in volume, as was possible to determine using μ -CT. Moreover, an expansion of nearly 3% in the FEBEX bentonite and 5% in the MX-80 bentonite could be quantified due to swelling.

The decrease in the SSA in both bentonites along the whole block was caused by the mobilization of the FeCl_2 due to the bentonite's porosity and, presumably, the adsorption of oxy-hydroxides or the precipitation of neoformed iron silicates near the montmorillonite surface, as observed using SEM-EDX, and confirmed using XRD. The observations

performed using SEM-EDX confirmed the interactions of the FeCl_2 with the montmorillonite, showed the precipitation of Fe-Cl corrosion products, and evidenced chloritization processes, although these could not be firmly confirmed using XRD. The formation of Fe spicules or fibrous Fe silicates was reported according to SEM observations in a previous study of Fe–bentonite interaction [54].

The CEC decreased in both bentonites. This phenomenon is usually associated with montmorillonite dissolution or variations in the layer charge. However, the CEC decrease in the present study is not associated with montmorillonite dissolution because there was no evidence of this observed according to any of the analytical methods used in the present work. After 18 years of exposure to a C-steel heater at 100 °C in an in situ FEBEX experiment, a reduction in the CEC was noted in FEBEX bentonite [55]. The authors of the study attributed this phenomenon to one of the following: an increase in the smectite layer charge by means of the reduction of the FeIII-bearing smectite, which caused interlayer collapse, or the collapse of the clay particles, induced by a large ionic strength, which generally reduces the swelling pressure [56]. In the present study, the decrease in the CEC was almost constant in MX-80 in the whole bentonite column. In the FEBEX bentonite, the decrease was almost constant except in the section closest to the hydration zone; therefore, it could be attributed to a higher salinity due to the direct contact with the saline solution. Nevertheless, this was not confirmed, and other possible reactions, such as the fixation of the interlayer cations (Fe^{2+}), could have affected the CEC.

Dohrmann et al. [57] suggested the possibility of a reduction in the CEC due to the elevated temperature of the experiments and/or the formation of corrosion products in the bentonite matrix, creating alkaline conditions that could not be confirmed experimentally in the present study, as the pH could not be measured without altering the experimental redox conditions.

The enrichment in divalent montmorillonite, regarding the initially monovalent MX-80 bentonite, could be explained by the ion exchange between the soluble divalent cations (Fe(II), Ca, Mg) and exchangeable Na in the interlayer complex [37,58]. This exchange could be enhanced by the hydration and dissolution of soluble salts like gypsum and calcite, present in the original bentonite, and, for instance, the exchange of FeCl^+ complexes in the montmorillonite [59]. The precipitation of halite observed using SEM/EDX and confirmed using XRD, due to the high concentrations of chloride in the system, favored the exchange complex to counteract the cation charge for the divalent cation species.

The increase in Fe content within the montmorillonite structure could be elucidated according to various mechanisms, such as the adsorption within the interlayer via cation exchange, adsorption at the edge sites of the montmorillonite, or association with newly precipitated oxides [60]. Additionally, redox reactions may have been produced, leading to the precipitation of Fe^{III} oxides or mixed $\text{Fe}^{\text{II}}/\text{Fe}^{\text{III}}$ oxides. Soluble Fe^{2+} migrated into the bentonite, and as oxygen from the bentonite pores diffused into the FeCl_2 powder, the interaction of iron with oxygen could have resulted in oxidation and subsequent precipitation on the montmorillonite surface, forming iron (hydr)oxides, as observed. The use of FeCl_2 powder instead of Fe^0 powder or metal plates provided faster mobilization due to its solubility in water and the imposed hydrothermal gradient. This factor allowed a higher reactivity, with Fe interacting along the whole bentonite columns and not only in the mm closer to the heater, as occurred in more realistic experiments [22,29,61,62]. It is worth mentioning that initially, the monovalent MX-80 bentonite favored Fe^{2+} exchange and a more intense (in quantity) diffusion of the ion through the whole compacted bentonite material. The original divalent FEBEX bentonite allocated much less iron relative to MX-80, as shown by the EDX elemental profiles.

Determinations of the redox state of iron analyzed using the redox indicator 1,10-phenanthroline showed that Fe^{2+} was mainly concentrated in the middle sections of the bentonite block. This may be due to the oxidation of Fe^{2+} into Fe^{3+} in the sections close to the FeCl_2 , as the hydration solution moved from the upper part to the bottom, preferentially through the external boundaries of the bentonite column, and could have migrated, dissolving the initial

oxygen present in the bentonite pores, favoring oxidation conditions at the bottom of the cell. Wersin et al. [16] found that the iron in the zone closest to the heater was preferentially Fe^{3+} , which is consistent with the detection of hematite and goethite in this zone. Through the interaction with the bentonite, Fe^{2+} was oxidated partially into Fe^{3+} in the middle section of the bentonite block, coexisting with both species. However, the Fe^{3+} concentrations were much higher than those of Fe^{2+} , due to the oxidation of Fe^{2+} into Fe^{3+} [16].

Considering the Fe^{2+} and Fe^{3+} data obtained in the present study, a mass balance calculation over the whole bentonite column indicated that MX-80 increased in its overall Fe^{3+} content by 137%, decreasing, meanwhile, in its Fe^{2+} content by 42%. Consistently, the Fe^{3+} content in the FEBEX bentonite increased by 101%, but the Fe^{2+} also increased by 24%.

Considering the large amount of reactive iron introduced into the system in highly saline conditions, both bentonites presented a high mineralogical stability and also a large swelling capacity, as far as the initial macroporosity of the bentonites was reduced in both experiments due to their swelling capacities. Not many differences were found in their response to aggressive conditions, but a higher net increase in Fe was observed using EDX analyses in the MX-80 bentonite, and a larger conversion of FeII into FeIII. The identification of newly formed minerals in the bentonites was very limited to the contact with the FeCl_2 and barely distinguishable in some cases, but green rust, ankerite, and hematite corrosion products were found in both bentonites, and iron-containing particles were observed using SEM, covering the clay surfaces. Goethite, also considered a corrosion product, was observed not only at the interface with the FeCl_2 but up to 15 mm from the interface. Additionally, pyrite and a Fe-rich chlorite phase were detected in MX-80.

Due to the use of FeCl_2 , the content in Cl^- increased considerably, as determined in all samples in the aqueous extracts. The XRD powder analyses showed akaganeite as an oxyhydroxide iron with chloride and hydrated iron chloride. In the MX-80 bentonite, Cl was also present in halite. Ankerite was slightly detected using XRD in the section closest to the heater. These minerals had been reported by Acosta et al. [63], supporting that Ca^{2+} could interact with Fe^{2+} and form ankerite if there was CaCO_3 in the medium. Raw bentonite had calcite as an accessory mineral. This hypothesis was not confirmed according to the other techniques in this work. The formation of green rust, observed using XRD in both bentonites, MX-80 and FEBEX, near the interface with FeCl_2 was indicative of local reducing conditions, which occur when the oxygen initially present in the air-filled gaps and pores of bentonite has been consumed and has been associated, in similar studies, to the formation of magnetite and siderite, via the reduction of previously formed Fe(III) oxides (e.g., [16]). The SEM/EDX analyses revealed the presence of polygonal pyrite framboids in the MX-80 bentonite at the contact with the FeCl_2 . The formation of this secondary mineral was also observed in [36] and suggested the likelihood of local reducing conditions. This presence of pyrite differs from that determined using XRD throughout the whole MX-80 bentonite column, which was initially present as an accessory mineral. Alternatively, pyrite formation could indicate the presence of sulfate-reducing bacteria capable of reducing the sulfates from the porewater, which seems implausible since the activity of these microorganisms at elevated temperatures is unlikely to occur and was not observed in bentonite samples from an in situ FEBEX experiment heater [64].

5. Conclusions

The experimental design facilitated the study of the hydrothermal alterations in bentonites and investigation of the impacts produced by the use of iron(II) chloride powder as the source of soluble iron, instead of steel or iron powder, designed to mimic an EBS system, as it is considered in a real scenario.

The main consequence observed due to the hydrothermal gradient after 6 months was the partial dissolution of the FeCl_2 powder in the studied cells and its diffusion through the bentonites. Iron II and III chlorides were redistributed and precipitated in addition to halite, favored by evidence of the Na exchanged by the divalent cations, although this was

not experimentally determined. Iron oxides with akaganeite were identified near the heat source with the detection of small amounts of serpentine-like minerals.

Considering the large amount of reactive iron introduced into the system in highly saline conditions, both bentonites presented high mineralogical stability and also a large swelling capacity, as far as the initial macroporosity of the bentonites was reduced in both experiments due to their swelling capacities. Not many differences were found in their response to aggressive conditions, but a higher net increase in Fe was observed according to the EDX analyses in the MX-80 bentonite, and a larger conversion of FeII into FeIII. The identification of newly formed minerals in bentonite was very limited to the contact with the FeCl₂ and barely distinguishable in some cases, but green rust, ankerite, and hematite corrosion products were found in both bentonites, and iron-containing particles were observed using SEM, covering the clay surfaces. Goethite, also considered a corrosion product, was observed not only at the interface with the FeCl₂ but up to 15 mm from the interface. Additionally, pyrite and a Fe-rich chlorite phase were detected in MX-80.

The effects of FeCl₂'s interaction with both bentonites resulted in a decrease in the specific surface area and cation exchange capacity.

The nature of the unsaturated compacted bentonites and the fluid transport through the cells possibly generated more oxic conditions than initially expected. Nevertheless, this study provides valuable insights into the intricate interactions and modifications that occur in bentonites subjected to FeCl₂ alteration hydrothermal conditions, revealing the influence of the different bentonites used. The use of FeCl₂ as the soluble iron emphasizes the complexity of these processes and insists on the need for a thorough understanding in the context of waste repository design and management. The geochemical processes and mineral phases observed in the present work could be useful for improving geochemical modeling studies, including the decrease in the CEC and SSA, the increase in water content and swelling, and the local redox environments required for the precipitation of secondary minerals.

Supplementary Materials: The following supporting information can be downloaded at <https://www.mdpi.com/article/10.3390/min14020132/s1>, Video S1: MX-80 FeCl₂ T0, Video S2: MX-80 FeCl₂ T6, Video S3: FEBEX FeCl₂ T0, Video S4: FEBEX FeCl₂ T6.

Author Contributions: Conceptualization, C.M.-H., R.F. and J.C.; methodology, C.M.-H., R.F. and J.C.; software, C.M.-H., R.F. and J.C.; validation, R.F. and J.C.; formal analysis, C.M.-H.; investigation, C.M.-H., R.F. and J.C.; resources, C.M.-H., R.F. and J.C.; data curation, C.M.-H., R.F. and J.C.; writing—original draft preparation, C.M.-H.; writing—review and editing, R.F., J.C. and C.M.-H.; visualization, C.M.-H., R.F. and J.C.; supervision, R.F. and J.C.; project administration, J.C.; funding acquisition, J.C. All authors have read and agreed to the published version of the manuscript.

Funding: This research belongs to the EURAD-ACED project, which has received funding from the European Union's Horizon 2020 research and innovation program under grant agreement no. 847593.

Data Availability Statement: Data are available on request from the authors.

Acknowledgments: The authors acknowledge María del Pilar Padilla Encinas for her help and production of the μ -CT videos and images.

Conflicts of Interest: The authors declare no conflict of interest.

References

1. Bergaya, F.; Lagaly, G. Chapter 1—General Introduction: Clays, Clay Minerals, and Clay Science. In *Developments in Clay Science*; Bergaya, F., Lagaly, G., Eds.; Elsevier: Amsterdam, The Netherlands, 2013; Volume 5, pp. 1–19. ISBN 1572-4352.
2. Brigatti, M.F.; Galán, E.; Theng, B.K.G. Chapter 2—Structure and Mineralogy of Clay Minerals. In *Developments in Clay Science*; Bergaya, F., Lagaly, G., Eds.; Elsevier: Amsterdam, The Netherlands, 2013; Volume 5, pp. 21–81. ISBN 1572-4352.
3. Schoonheydt, R.A.; Johnston, C.T. Chapter 5—Surface and Interface Chemistry of Clay Minerals. In *Developments in Clay Science*; Bergaya, F., Lagaly, G., Eds.; Elsevier: Amsterdam, The Netherlands, 2013; Volume 5, pp. 139–172. ISBN 1572-4352.
4. Svensson, D. The Bentonite Barrier—Swelling Properties, Redox Chemistry and Mineral Evolution. Ph.D. Thesis, Centre for Analysis and Synthesis, Department of Chemistry, Faculty of Engineering, LTH Lund University, Lund, Sweden, 2015.

5. Villar, M.V. *Thermo-Hydro-Mechanical Characterisation of a Bentonite from Cabo de Gata. A Study Applied to the Use of Bentonite as a Sealing Material in High Level Waste Repositories*; ENRESA: Madrid, Spain, 2002; p. 277.
6. ENRESA. *Evaluación del Comportamiento y de la Seguridad de un Almacenamiento Geológico Profundo en Granito*; ENRESA: Madrid, Spain, 1997; p. 179.
7. Bildstein, O.; Claret, F. Chapter 5—Stability of Clay Barriers Under Chemical Perturbations. In *Natural and Engineered Clay Barriers*; Tournassat, C., Steefel, C.I., Bourg, I.C., Bergaya, F., Eds.; Developments in Clay Science; Elsevier: Amsterdam, The Netherlands, 2015; Volume 6, pp. 155–188.
8. Wu, J.; Low, P.F.; Roth, C.B. Effects of Octahedral-Iron Reduction and Swelling Pressure on Interlayer Distances in Na-Nontronite. *Clays Clay Miner.* **1989**, *37*, 211–218.
9. Stucki, J.W. A Review of the Effects of Iron Redox Cycles on Smectite Properties. *Comptes Rendus Geosci.* **2011**, *343*, 199–209. [[CrossRef](#)]
10. Hofstetter, T.B.; Sosedova, Y.; Gorski, C.; Voegelin, A.; Sander, M. *Redox Properties of Iron-Bearing Clays and MX-80 Bentonite—Electrochemical and Spectroscopic Characterization*; NAGRA: Wettingen, Switzerland, 2014; p. 50.
11. Stucki, J.W. Chapter 11—Properties and Behaviour of Iron in Clay Minerals. In *Developments in Clay Science*; Bergaya, F., Lagaly, G., Eds.; Elsevier: Amsterdam, The Netherlands, 2013; Volume 5, pp. 559–611.
12. Necib, S.; Linard, Y.; Crusset, D.; Michau, N.; Daumas, S.; Burger, E.; Romaine, A.; Schlegel, M.L. Corrosion at the Carbon Steel clay Borehole Water and Gas Interfaces at 85 °C under Anoxic and Transient Acidic Conditions. *Corros. Sci.* **2016**, *111*, 242–258. [[CrossRef](#)]
13. NUMO. *Safety of the Geological Disposal Project 2010*; NUMO: Tokyo, Japan, 2013; p. 148.
14. King, F.; Ahonen, L.; Taxén, C.; Vuorinen, U.; Werme, L. *Copper Corrosion under Expected Conditions in a Deep Geologic Repository*; POSIVA OY: Helsinki, Finland, 2002; p. 184.
15. Reddy, B.; Padovani, C.; Rance, A.P.; Smart, N.R.; Cook, A.; Haynes, H.M.; Milodowski, A.E.; Field, L.P.; Kemp, S.J.; Martin, A.; et al. The Anaerobic Corrosion of Candidate Disposal Canister Materials in Compacted Bentonite Exposed to Natural Granitic Porewater Containing Native Microbial Populations. *Mater. Corros.* **2021**, *72*, 361–382. [[CrossRef](#)]
16. Wersin, P.; Kober, F. *FEBEX-DP Metal Corrosion and Iron-Bentonite Interaction Studies*; NAGRA: Wettingen, Switzerland, 2017; p. 300.
17. Li, Z.; Chanéac, C.; Berger, G.; Delaunay, S.; Graff, A.; Lefèvre, G. Mechanism and Kinetics of Magnetite Oxidation under Hydrothermal Conditions. *RSC Adv.* **2019**, *9*, 33633–33642. [[CrossRef](#)] [[PubMed](#)]
18. Zhao, J.; Brugger, J.; Pring, A. Mechanism and Kinetics of Hydrothermal Replacement of Magnetite by Hematite. *Geosci. Front.* **2019**, *10*, 29–41. [[CrossRef](#)]
19. Aragonese, F.J.; García-González, M.T. High-Charge Smectite in Spanish “Raña” Soils. *Clays Clay Miner.* **1991**, *39*, 211–218. [[CrossRef](#)]
20. Schwertmann, U. Solubility and Dissolution of Iron Oxides. *Plant Soil* **1991**, *130*, 1–25. [[CrossRef](#)]
21. Wilson, J.; Savage, D.; Cuadros, J.; Shibata, M.; Ragnarsdottir, K.V. The Effect of Iron on Montmorillonite Stability. (I) Background and Thermodynamic Considerations. *Geochim. Cosmochim. Acta* **2006**, *70*, 306–322. [[CrossRef](#)]
22. Hadi, J.; Wersin, P.; Serneels, V.; Greneche, J.-M. Eighteen Years of Steel–Bentonite Interaction in the FEBEX in Situ Test at the Grimsel Test Site in Switzerland. *Clays Clay Miner.* **2019**, *67*, 111–131. [[CrossRef](#)]
23. Kumpulainen, S.; Kiviranta, L.; Korkeakoski, P. Long-Term Effects of an Iron Heater and Äspö Groundwater on Smectite Clays: Chemical and Hydromechanical Results from the in Situ Alternative Buffer Material (ABM) Test Package 2. *Clay Miner.* **2016**, *51*, 129–144. [[CrossRef](#)]
24. Torres, E.; Turrero, M.J.; Moreno, D.; Sánchez, L.; Garralón, A. FEBEX In-Situ Test: Preliminary Results of the Geochemical Characterization of the Metal/Bentonite Interface. *Procedia Earth Planet. Sci.* **2017**, *17*, 802–805. [[CrossRef](#)]
25. Kaufhold, S.; Hassel, A.W.; Sanders, D.; Dohrmann, R. Corrosion of High-Level Radioactive Waste Iron-Canisters in Contact with Bentonite. *J. Hazard. Mater.* **2015**, *285*, 464–473. [[CrossRef](#)] [[PubMed](#)]
26. Gómez-Espina, R.; Villar, M.V. Effects of Heat and Humidity Gradients on MX-80 Bentonite Geochemistry and Mineralogy. *Appl. Clay Sci.* **2015**, *109–110*, 39–48. [[CrossRef](#)]
27. Wersin, P.; Hadi, J.; Kiczka, M.; Jenni, A.; Grenèche, J.-M.; Diomidis, N.; Leupin, O.X.; Svensson, D.; Sellin, P.; Reddy, B.; et al. Unravelling the Corrosion Processes at Steel/Bentonite Interfaces in in Situ Tests. *Mater. Corros.* **2023**, *74*, 1716–1727. [[CrossRef](#)]
28. Carlson, L.; Karnland, O.; Oversby, V.M.; Rance, A.P.; Smart, N.R.; Snellman, M.; Vähänen, M.; Werme, L.O. Experimental Studies of the Interactions between Anaerobically Corroding Iron and Bentonite. *Phys. Chem. Earth Parts A/B/C* **2007**, *32*, 334–345. [[CrossRef](#)]
29. Hadi, J.; Wersin, P.; Jenni, A.; Greneche, J.M. *Redox Evolution and Fe-Bentonite Interaction in the ABM2 Experiment, Äspö Hard Rock Laboratory*; NAGRA: Wettingen, Switzerland, 2017; p. 330.
30. Smart, N.R.; Reddy, B.; Rance, A.P.; Nixon, D.J.; Diomidis, N. The Anaerobic Corrosion of Carbon Steel in Saturated Compacted Bentonite in the Swiss Repository Concept. *Corros. Eng. Sci. Technol.* **2017**, *52*, 113–126. [[CrossRef](#)]
31. Leupin, O.X.; Smart, N.R.; Zhang, Z.; Stefanoni, M.; Angst, U.; Papafotiou, A.; Diomidis, N. Anaerobic Corrosion of Carbon Steel in Bentonite: An Evolving Interface. *Corros. Sci.* **2021**, *187*, 109523. [[CrossRef](#)]
32. Wilson, J.C.; Benbow, S.; Sasamoto, H.; Savage, D.; Watson, C. Thermodynamic and Fully-Coupled Reactive Transport Models of a Steel-Bentonite Interface. *Appl. Geochem.* **2015**, *61*, 10–28. [[CrossRef](#)]

33. Xia, X.; Idemitsu, K.; Arima, T.; Inagaki, Y.; Ishidera, T.; Kurosawa, S.; Iijima, K.; Sato, H. Corrosion of Carbon Steel in Compacted Bentonite and Its Effect on Neptunium Diffusion under Reducing Condition. *Appl. Clay Sci.* **2005**, *28*, 89–100. [[CrossRef](#)]
34. Géhin, A.; Grenèche, J.-M.; Tournassat, C.; Brendlé, J.; Rancourt, D.G.; Charlet, L. Reversible Surface-Sorption-Induced Electron-Transfer Oxidation of Fe(II) at Reactive Sites on a Synthetic Clay Mineral. *Geochim. Cosmochim. Acta* **2007**, *71*, 863–876. [[CrossRef](#)]
35. Kamei, G.; Oda, C.; Mitsui, S.; Shibata, M.; Shinozaki, T. Fe(II)–Na Ion Exchange at Interlayers of Smectite: Adsorption–Desorption Experiments and a Natural Analogue. *Eng. Geol.* **1999**, *54*, 15–20. [[CrossRef](#)]
36. Duro, L.; Bruno, J.; Grivé, M.; Montoya, V.; Kienzler, B.; Altmaier, M.; Buckau, G. Redox Processes in the Safety Case of Deep Geological Repositories of Radioactive Wastes. Contribution of the European RECOZY Collaborative Project. *Appl. Geochem.* **2014**, *49*, 206–217. [[CrossRef](#)]
37. Mota-Heredia, C.; Cuevas, J.; Ruiz, A.I.; Ortega, A.; Torres, E.; Turrero, M.J.; Fernández, R. Geochemical Interactions at the Steel-Bentonite Interface Caused by a Hydrothermal Gradient. *Appl. Clay Sci.* **2023**, *240*, 106984. [[CrossRef](#)]
38. Bradbury, M.H.; Baeyens, B. Porewater Chemistry in Compacted Re-Saturated MX-80 Bentonite. *J. Contam. Hydrol.* **2003**, *61*, 329–338. [[CrossRef](#)] [[PubMed](#)]
39. Bradbury, M.H.; Baeyens, B. Experimental and Modelling Studies on the pH Buffering of MX-80 Bentonite Porewater. *Appl. Geochem.* **2009**, *24*, 419–425. [[CrossRef](#)]
40. Montes-H, G.; Fritz, B.; Clement, A.; Michau, N. Modelling of Geochemical Reactions and Experimental Cation Exchange in MX80 Bentonite. *J. Environ. Manag.* **2005**, *77*, 35–46. [[CrossRef](#)] [[PubMed](#)]
41. Jönsson, B.; Åkesson, T.; Jönsson, B.; Meehdi, S.; Janiak, J.; Wallenberg, R. *Structure and Forces in Bentonite MX-80*; Theoretical Chemistry, Chemical Center: Sweden, Switzerland, 2009; p. 34.
42. Caballero, E.; Jiménez de Cisneros, C.; Huertas, F.J.; Huertas, F.; Pozzuoli, A.; Linares, J. Bentonites from Cabo de Gata, Almeria, Spain: A Mineralogical and Geochemical Overview. *Clay Miner.* **2005**, *40*, 463–480. [[CrossRef](#)]
43. Fernández, A.M.; Baeyens, B.; Bradbury, M.; Rivas, P. Analysis of the Porewater Chemical Composition of a Spanish Compacted Bentonite Used in an Engineered Barrier. *Phys. Chem. Earth* **2004**, *29*, 105–118. [[CrossRef](#)]
44. FEBEX. *Bentonite: Origin, Properties and Fabrication of Blocks*; ENRESA: Madrid, Spain, 1998; Volume PT-4/98.
45. Cuevas, J.; Cabrera, M.Á.; Fernández, C.; Mota-Heredia, C.; Fernández, R.; Torres, E.; Turrero, M.J.; Ruiz, A.I. Bentonite Powder XRD Quantitative Analysis Using Rietveld Refinement: Revisiting and Updating Bulk Semiquantitative Mineralogical Compositions. *Minerals* **2022**, *12*, 772. [[CrossRef](#)]
46. Cuevas, J.; Ruiz, A.I.; Fernández, R.; Torres, E.; Escribano, A.; Regadío, M.; Turrero, M.J. Lime Mortar-Compacted Bentonite–Magnetite Interfaces: An Experimental Study Focused on the Understanding of the EBS Long-Term Performance for High-Level Nuclear Waste Isolation DGR Concept. *Appl. Clay Sci.* **2016**, *124–125*, 79–93. [[CrossRef](#)]
47. Meier, L.P.; Kahr, G. Determination of the cation exchange capacity (CEC) of clay minerals using the complexes of copper(II) ion with triethylenetetramine and tetraethylenepentamine. *Clays Clay Miner.* **1999**, *47*, 386–388. [[CrossRef](#)]
48. Ammann, L.; Bergaya, F.; Lagaly, G. Determination of the Cation Exchange Capacity of Clays with Copper Complexes Revisited. *Clay Miner.* **2005**, *40*, 441–455. [[CrossRef](#)]
49. Stucki, J.W. The Quantitative Assay of Minerals for Fe²⁺ and Fe³⁺ Using 1,10-Phenanthroline: II. A Photochemical Method. *Soil Sci. Soc. Am. J.* **1981**, *45*, 638–641. [[CrossRef](#)]
50. Stucki, J.W.; Anderson, W.L. The Quantitative Assay of Minerals for Fe²⁺ and Fe³⁺ Using 1,10-Phenanthroline: I. Sources of Variability. *Soil Sci. Soc. Am. J.* **1981**, *45*, 633–637. [[CrossRef](#)]
51. Hillier, S.; Velde, B. Chlorite Interstratified with a 7 Å Mineral: An Example from Offshore Norway and Possible Implications for the Interpretation of the Composition of Diagenetic Chlorites. *Clay Miner.* **1992**, *27*, 475–486. [[CrossRef](#)]
52. Xu, H.; Veblen, D.R. Interstratification and Other Reaction Microstructures in the Chlorite-Berthierine Series. *Contributions to Mineral. Petrol.* **1996**, *124*, 291–301. [[CrossRef](#)]
53. Villar, M.V.; Martín, P.L.; Bárcena, I.; García-Siñeriz, J.L.; Gómez-Espina, R.; Lloret, A. Long-Term Experimental Evidences of Saturation of Compacted Bentonite under Repository Conditions. *Eng. Geol.* **2012**, *149–150*, 57–69. [[CrossRef](#)]
54. Kaufhold, S.; Schippers, A.; Marx, A.; Dohrmann, R. SEM Study of the Early Stages of Fe-Bentonite Corrosion—The Role of Naturally Present Reactive Silica. *Corros. Sci.* **2020**, *171*, 108716. [[CrossRef](#)]
55. Fernández, A.M.; Kaufhold, S.; Sánchez-Ledesma, D.M.; Rey, J.J.; Melón, A.; Robredo, L.M.; Fernández, S.; Labajo, M.A.; Clavero, M.A. Evolution of the THC Conditions in the FEBEX in Situ Test after 18 Years of Experiment: Smectite Crystallochemical Modifications after Interactions of the Bentonite with a C-Steel Heater at 100 °C. *Appl. Geochem.* **2018**, *98*, 152–171. [[CrossRef](#)]
56. Herbert, H.-J.; Kasbohm, J.; Sprenger, H.; Fernández, A.M.; Reichelt, C. Swelling Pressures of MX-80 Bentonite in Solutions of Different Ionic Strength. *Phys. Chem. Earth Parts A/B/C* **2008**, *33*, S327–S342. [[CrossRef](#)]
57. Dohrmann, R.; Kaufhold, S. Cation Exchange and Mineral Reactions Observed in MX 80 Buffer Samples of the Prototype Repository In Situ Experiment in Äspö, Sweden. *Clays Clay Miner.* **2014**, *62*, 357–373. [[CrossRef](#)]
58. Fernández, A.M.; Marco, J.F.; Nieto, P.; León, F.J.; Robredo, L.M.; Clavero, M.Á.; Cardona, A.I.; Fernández, S.; Svensson, D.; Sellin, P. Characterization of Bentonites from the In Situ ABM5 Heater Experiment at Äspö Hard Rock Laboratory, Sweden. *Minerals* **2022**, *12*, 471. [[CrossRef](#)]
59. Charlet, L.; Tournassat, C. Fe(II)-Na(I)-Ca(II) Cation Exchange on Montmorillonite in Chloride Medium: Evidence for Preferential Clay Adsorption of Chloride—Metal Ion Pairs in Seawater. *Aquat. Geochem.* **2005**, *11*, 115–137. [[CrossRef](#)]

60. Wersin, P.; Jebril, H.; Jenni, A.; Svensson, D.; Jean-Marc, G.; Sellin, P.; Leupin, O.X. Interaction of Corroding Iron with Eight Bentonites in the Alternative Buffer Materials Field Experiment (ABM2). *Minerals* **2021**, *11*, 907. [[CrossRef](#)]
61. Uyama, M.; Hitomi, T.; Hayagane, S.; Kadota, N.; Saito, H.; Okamoto, S.; Aoshima, K.; Osawa, M. Analysis of Corrosion Mechanisms of Carbon Steel in Contact with FEBEX Bentonite. *Geol. Soc. Lond. Spec. Publ.* **2019**, *482*, 301–312. [[CrossRef](#)]
62. Wersin, P.; Jenni, A.; Mäder, U.K. Interaction of Corroding Iron with Bentonite in the ABM1 Experiment at Äspö, Sweden: A Microscopic Approach. *Clays Clay Miner.* **2015**, *63*, 51–68. [[CrossRef](#)]
63. Acosta, V.V.; Bianchi, G.L. Effects of Ca²⁺ Ions on the Localized Corrosion of Carbon Steel Influence of the Associated Anion. *Appl. Sci.* **2023**, *13*, 11056. [[CrossRef](#)]
64. Bengtsson, A.; Blom, A.; Taborowski, T.; Schippers, A.; Edlund, J.; Kalinowski, B.; Pedersen, K. *FEBEX-DP: Microbiological Report*; Nagra Working Report (No. 16–15); National Cooperative for the Disposal of Radioactive Waste: Wettingen, Switzerland, 2017.

Disclaimer/Publisher’s Note: The statements, opinions and data contained in all publications are solely those of the individual author(s) and contributor(s) and not of MDPI and/or the editor(s). MDPI and/or the editor(s) disclaim responsibility for any injury to people or property resulting from any ideas, methods, instructions or products referred to in the content.